Actinium and radium fluxes from the seabed in the northeast Pacific Basin

Nathaniel Kemnitz [a,*], Douglas E. Hammond [a], Paul Henderson [b], Emilie Le Roy [b], Matthew Charette [b], Willard Moore [c], Robert F. Anderson [d], Martin Q. Fleisher [d], Anne Leal [d], Erin Black [e], Christopher T. Hayes [f], Jess Adkins [g], William Berelson [a], Xiaopeng Bian [a]

[a] *University of Southern California, Los Angeles, CA, United States of America*
[b] *Woods Hole Oceanographic Institution, Woods Hole, MA, United States of America*
[c] *University of South Carolina, Columbia, SC, United States of America*
[d] *Lamont-Doherty Earth Observatory, Palisades, NY, United States of America*
[e] *University of Rochester, Rochester, NY, United States of America*
[f] *University of Southern Mississippi, Hattiesburg, MS, United States of America*
[g] *California Institute of Technology, Pasadena, CA, United States of America*

ARTICLE INFO

ABSTRACT

Five sediment cores were collected along a cruise tract from Hawaii to Alaska in August 2017 (C-Disk-IV cruise) with the objective of characterizing the behavior of ^{227}Ac, ^{228}Ra, and ^{226}Ra and their fluxes into the overlying water column, information that is essential to the interpretation of the distribution of these tracers in the ocean, for example, as measured on GEOTRACES cruises. Solid phase profiles of these isotopes were measured, and reaction-transport models were applied that incorporated molecular diffusion, bioturbation, sedimentation, distribution coefficients (k_d), and the fraction of each isotope released to pore water by parent decay (called F). Fits to these profiles used k_d values determined in lab experiments for C-Disk-IV sediments. Ra k_d values (1000–3000 mL g^{-1}) agreed with previous estimates for deep-sea sediments, and Ac k_d values (3500–22,000 mL g^{-1}) correlated with those for Ra but were about 7 times greater.

Two independent approaches were used to quantify the benthic fluxes of ^{227}Ac and ^{228}Ra in the Northeast Pacific: (1) use of solid phase profiles with a reaction-transport model, as well as integrated downcore daughter-parent deficiency; and (2) direct measurement of fluxes based on core incubation. The two independent methods agreed within uncertainty, and the average ^{227}Ac and ^{228}Ra sediment fluxes for the Northeast Pacific are 90 ± 20 and 600 ± 200 dpm m^{-2}-yr^{-1}, respectively. The ^{226}Ra sediment flux was only determined by the former approach, and the flux calculated in this study is similar to previous work in the North Pacific, averaging 1300 ± 200 dpm m^{-2}-yr^{-1}. This is over $2\times$ higher than the water column inventory of ^{226}Ra in this region (600 dpm m^{-2}-yr^{-1}), and indicates the importance of lateral ^{226}Ra export from the N. Pacific.

The largest ^{227}Ac and Ra isotope fluxes in the study area are near the center of the Northeast Pacific ($\sim37°$N). Smaller ^{227}Ac, ^{228}Ra and ^{226}Ra fluxes occur north of $40°$N, primarily due to dilution of their Pa and Th ancestors by higher sediment accumulation rates.

1. Introduction

^{227}Ac ($t_{1/2} = 21.77$ y) has shown potential as a tracer for mixing on the basin scale range (Nozaki, 1984; Nozaki et al., 1990; Geibert and Vöge, 2008; Geibert et al., 2002). Nozaki first proposed ^{227}Ac as a deep-sea tracer in 1984, but for years, ^{227}Ac went relatively unmeasured due to its low concentrations and difficulties with detection in ocean sediments and waters (Geibert and Vöge, 2008). However, during the last

30 years, better methods have evolved that can measure small concentrations of this isotope, due to development of the Radium Delayed Coincidence Counters (RaDeCC; Moore and Arnold, 1996; Shaw and Moore, 2002; Dulaiova et al., 2012), and more sensitive mass spectrometers (Levier et al., 2021).

GEOTRACES is an international collaboration whose main objective is to understand the processes that control the distribution and transport of trace elements and isotopes (TEIs) in the oceans (GEOTRACES

Planning Group, 2007). One important component for understanding these processes is quantifying transport using naturally occurring radioisotopes, including ^{228}Ra and ^{227}Ac. The last 4 US GEOTRACES section cruises (GA03, GP16, GN01, GP15) have collected Ra and Ac from seawater by pumping large volumes through acrylic fibers impregnated with MnO$_2$. This has led to acquisition of a number of data sets for the radium quartet (^{223}Ra, ^{224}Ra, ^{228}Ra, and ^{226}Ra) and ^{227}Ac distribution throughout the oceans. High resolution sampling has occurred in the North Atlantic, North and South Pacific, and the Arctic oceans (Charette et al., 2015, Kipp et al., 2018; Sanial et al., 2018; Hammond et al., in prep; Kemnitz et al., in prep). Applying these isotopes as tracers can be facilitated if their source functions are defined. While ^{226}Ra and ^{228}Ra in deep ocean sediments have been well studied at several locations to constrain their source functions, limited data exists for ^{227}Ac (Cochran and Krishnaswami, 1980; Kadko, 1980; Nozaki et al., 1990; Moore et al., 1996; Rama and Moore, 1996; Kipp et al., 2018; van der Loeff et al., 2018). This limits its utility (Ku and Luo, 2008). A few studies have assumed mass balance models (Geibert et al., 2008), but Nozaki et al. (1990) is the only study to date to have directly measured ^{227}Ac in sediments. Thus, this study aims to improve knowledge of the geochemical behavior of ^{227}Ac, ^{226}Ra, and ^{228}Ra in marine sediments and estimate their fluxes into deep ocean waters.

One objective of this study is to compare methodologies to measure ^{227}Ac fluxes from marine sediments by using two independent methods: indirectly by modeling solid phase profile activity measurements and directly by core incubations. The former approach utilizes previously published reactive-transport models to predict geochemical behaviors of ^{227}Ac and other radionuclides (^{226}Ra & ^{228}Ra) in the sediments sampled during this study, while the second approach has not previously been utilized in the deep sea. A second objective is to evaluate spatial variability in sediment fluxes for ^{227}Ac, ^{228}Ra, and ^{226}Ra in a section through the Northeast Pacific Basin (NEPB) and show how the water column distribution of these radionuclides is related to these fluxes.

2. Theory

Cochran and Krishnaswami (1980) developed a reactive transport model for the behavior of ^{226}Ra and ^{228}Ra in marine sediments. This model can be adapted for ^{227}Ac as well (Nozaki et al., 1990). The model assumes parents of these isotopes are associated with solids, while one fraction of the more mobile daughters may diffuse as solutes or reversibly adsorb to solid phases, and a second fraction of these daughters is tightly bound within solid phases and does not exchange with the fluid phase. This model is idealized, but accounts for the major processes that govern reaction and transport in sediments, including molecular diffusion, radioactive decay, burial, and bioturbation (treated as a diffusive process). Sediments are divided into an upper, bioturbated layer that overlies a deeper layer that is no longer bioturbated. The governing one-dimensional steady state equations are given by:

$$\frac{\partial C}{\partial t} = (D_s + KD_b)\frac{\partial^2 C}{\partial z^2} - S(1+K)\frac{\partial C}{\partial z} - \lambda(1+K)C + P = 0 \; for \; 0 \le z \le L \tag{1a}$$

$$\frac{\partial C}{\partial t} = D_s \frac{\partial^2 C}{\partial z^2} - S(1+K)\frac{\partial C}{\partial z} - \lambda(1+K)C + P = 0 \; for \; z \ge L \tag{1b}$$

where:C = concentration of dissolved radioisotope in porewater (atoms cm^{-3}).D_s = molecular diffusion corrected for tortuosity (cm^2 yr^{-1}).D_b = bioturbation (cm^2 yr^{-1}); assumed constant in the upper layer.S = sedimentation rate (cm yr^{-1}).λ = decay constant of daughter (yr^{-1}).P = production rate of daughter atoms per unit of porewater from parent decay (atoms cm^{-3} yr^{-1}).K = partition coefficient (dimensionless).z = depth in sediments (cm).L = thickness of bioturbation zone (cm).

A solution to Eq. (1a) assumes sedimentation rate, molecular diffusion, and K are all constant and independent with respect to depth;

bioturbation is constant in the upper layer (Cochran and Krishnaswami, 1980; Kadko, 1980). Solid phase ^{231}Pa and ^{230}Th profiles in the bioturbated layer (shown later) have been homogenized throughout the upper 6–8 cm. The production term (P) can be further expanded and expressed as:

$$P = FA_{p1} + fA_{p2} \; for \; 0 \le z \le L \tag{2a}$$

$$P = FA_{p1}e^{-\mu(z-L)} + fA_{p2} \; for \; z \ge L \tag{2b}$$

where:F = fraction of parent isotope (^{231}Pa or ^{230}Th) decays which recoil daughter products into porewater.f = fraction of grandparent isotope (^{235}U or ^{234}U) decays which recoil daughter products into porewater.A_{p1} = parent activity in solid multiplied by bulk density and divided by porosity to give equivalent activity per unit of porewater in atoms cm^{-3} yr^{-1}.A_{p2} = grandparent activity defined similarly to A_{p1}.

$$\mu = \frac{\lambda_p}{S} \; (cm^{-1})$$

λ_p=decay constant of parent.

Note: The grandparent-parent pair for A_{p1} and A_{p2} is assumed to be in equilibrium and f is typically minor, due to ^{234}U and ^{235}U being within a crystal lattice and having limited ability to recoil daughter products into porewater. The parent and grandparent activities per unit of porewater are calculated from solid phase activity multiplied by solid phase grams per cm^{-3} of porewater, based on porosity. Substituting Eqs. (2a) into (1a), solving for the concentration, multiplying by λ_d, and expressing concentrations as activities ($\lambda C = A$):

$$A_1(z) = Q_1 e^{\alpha_1 z} + R_1 e^{\delta_1 z} + \frac{FA_{p1} + fA_{p2}}{1+K} \; for \; 0 \le z \le L \tag{3a}$$

$$A_2(z) = Q_2 e^{\alpha_2 z} + \frac{FA_{p1}\lambda}{D_1}e^{-\mu(z-L)} + \frac{fA_{p2}}{1+K} \; for \; z \ge L \tag{3b}$$

where Q, R, α, and δ are all constants that depend on D$_s$, D$_b$, S, and K (See SI S.1 for full definition of these terms). A_{p1} is the parent activity of for a specific daughter in dpm cm^{-3} of porewater, A_{p2} is its grandparent activity in dpm cm^{-3} of porewater, A_1 is the porewater activity of this daughter in the bioturbated zone in dpm cm^{-3}, A_2 is the porewater activity of this daughter below the bioturbated zone in dpm cm^{-3}, A_0 is the concentration of daughter in porewater at the SWI (sediment-water interface) in dpm cm^{-3}, and z is depth in cm. Eq. (3a) depends on 4 boundary conditions:

1.) $at \; z = 0, A_1 = A_0$
2.) as z $\rightarrow \infty$, $A_2 \rightarrow \frac{fA_{p2}}{1+K}$
3.) $(A_1)_L = (A_2)_L$
4.) $D_s \left(\frac{\partial A_1}{\partial z}\right)_L = (D_s + KD_b)\left(\frac{\partial A_2}{\partial z}\right)_L$

To relate the dissolved concentration to the solid phase, the partition coefficient (K) can be related to the distribution coefficient, k$_d$ (in units of cm^3 g^{-1}) as:

$$K = \frac{k_d(1-\phi)\rho_s}{\phi} \tag{4}$$

where ρ_s = solid phase density (g cm^{-3}). k$_d$ relates the mobile solid and dissolved phase concentration C' (dpm g^{-1}) as:

$$k_d = \frac{C'}{C} \tag{5}$$

The following equations relate the dissolved phase (dpm cm^{-3}) to the solid phase (dpm g^{-1}) by multiplying Eq. (3a) by k$_d$ to find the mobile activity (dissolved plus adsorbed) and adding the immobile crystalline activity to obtain the total activity:

$$A_{1-tot}(z) = k_d(A_1) + (1-F)\left(A_{p1-tot} - A_{p2-tot}\right) + (1-f)A_{p2-tot} \; for \; 0 \leq z \leq L \tag{6a}$$

$$A_{2-tot}(z) = k_d(A_2) + (1-F)\left(A_{p1-tot} - A_{p2-tot}\right)e^{\mu(z-L)} + (1-f)A_{p2-tot} \; for \; z \geq L \tag{6b}$$

where A_{1-tot} and A_{2-tot} are the total activities of daughter products in the solid phase for each layer (dpm g^{-1}), A_{p1-tot} is the total parent activity for a specific daughter (^{231}Pa and ^{230}Th) in dpm g^{-1}, A_{p2-tot} is the total grandparent activity for this daughter (^{234}U and ^{235}U) in dpm g^{-1}, $(1-F)(A_{p1-tot} - A_{p2-tot})$ is the immobile fraction of ^{226}Ra or ^{227}Ac from excess ^{230}Th or ^{231}Pa decay (dpm g^{-1}), and $(1-f)A_{p2-tot}$ is the immobile fraction of ^{226}Ra or ^{227}Ac from ^{234}U/^{235}U decay (this decay is from within the crystal lattice of sediments).

Lastly, a one-layer model can be derived from Eq. (1a) if the parent activity and bioturbation are assumed constant throughout the entire profile. Due to its small scale-length, a one-layer model was used for ^{228}Ra in this study. Two boundary conditions were applied: at z = 0, the concentration of daughter products = A_0 and as z →∞, the concentration of daughter products → P/(1 + K), where P is parent activity. Solving for the concentrations with respect to the previous boundary conditions and expressing the concentrations as activities (A = λC):

$$A_D(z) = A_0 e^{-\alpha z} + \frac{P}{1+K}\left(1 - e^{-\alpha z}\right) \tag{7}$$

$$\alpha = \frac{-S(1+K) + \sqrt{\left(-S(1+K)\right)^2 + 4(D_s + KD_b)(\lambda_{Ac}(1+K))}}{2(D_s + KD_b)} \tag{8}$$

A_D = concentration of dissolved daughter in porewater (dpm cm^{-3}). A_0 = concentration of dissolved daughters in porewater at z = 0 (dpm cm^{-3}). P = activity of parent isotope (^{232}Th) per unit volume of porewater (dpm cm^{-3}).

For a one-layer model, the following equation relates the dissolved phase (dpm cm^{-3}) to the solid phase (dpm g^{-1}) by multiplying Eq. (7) by k_d and adding the total parent decay:

$$A'_{Total \; D}(z) = A_0 k_d e^{-\alpha z} + FA_{p1-tot}(1 - e^{-\alpha z}) + (1-F)A_{p1-tot} \tag{9}$$

$A_{Total \; D}$ = the total activity of daughters in solid phase (dpm g^{-1}).

Fluxes of ^{227}Ac, ^{226}Ra, or ^{228}Ra can be calculated by applying Fick's first law to the fitted equations:

$$Flux = -\left(D + D_b K\right)\phi \frac{dA}{dz} \tag{10}$$

where $\frac{dA}{dz}$ is the derivative of Eq. (6a) or (9).

3. Study area

Fig. 1 shows the C-Disk-IV (Carbonate Dissolution Kinetics-IV) and US GEOTRACES PMT (GP15) transects in the NEPB. All deep-sea sediment samples were collected during the C-Disk-IV Cruise aboard the R/V *Kilo Moana* in August 2017. Profiles of dissolved ^{227}Ac, ^{231}Pa, ^{226}Ra, and ^{228}Ra in the water column were collected during GP15 cruise aboard R/V *Roger Revelle* between September and November 2018.

Location, depth, surface porosity, sedimentation, and description of sediments for each C-Disk-IV station are summarized in Table 1. Stations 1, 2, and 3 are located within the subtropical gyre, where oligotrophic waters dominate, and organic export to the seafloor is low. The sediments at these stations are characterized by fine-grained, clay material with low organic content. Stations 4 and 5 are in the subarctic gyre, where primary production is high. Their sediments are characterized by larger grain size material with higher biogenic fraction in comparison to stations 1–3. A distinctive fluff layer was observed above the sediments
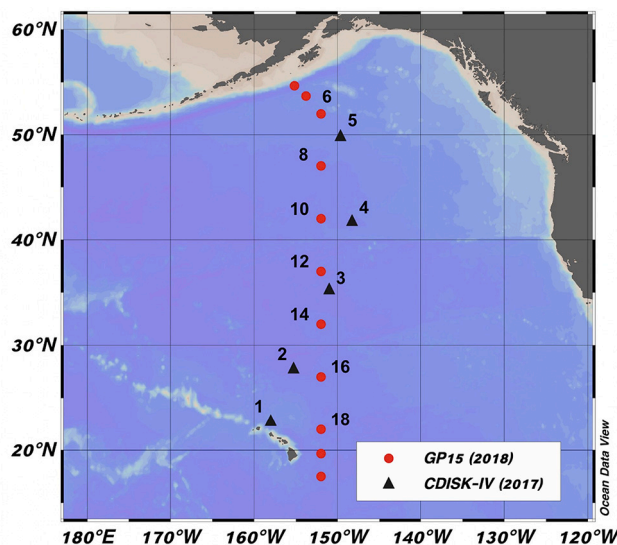

Fig. 1. Study area of the Northeast Pacific Basin (NEPB). Red dots and black triangles refer to stations where ^{227}Ac was measured in the water column for GEOTRACES PMT (GP15) and C-Disk-IV cruises. Numbers next to symbols refer to station numbers. All sediment isotope profiles (Ra, Th, Ac, Pb, and Po) were made on C-Disk-IV cruise samples. (For interpretation of the references to color in this figure legend, the reader is referred to the web version of this article.)

Table 1
Station information for C-Disk-IV cruise. Sediment description is taken from Hou et al. (2019). Porosity was estimated from water loss of sediments for top 3 cm. Density of sediments was assumed 2.5 g cm^{-3}. Linear sedimentation rates were found based on fits to the ^{226}Ra profiles below the mixed layer, as these reflect ^{230}Th profiles.

Station	Location	Bottom depth	Surface porosity	Sed. rate	Sediment description
	(°N, °W)	(m)	(%)	(cm kyr^{-1})	
1	22.8, 158.0	4730	86	0.44	uniform light reddish-brown color, tube/worm visible at the sediment surface
2	27.8, 155.2	5640	83	0.11	uniform light brown color, manganese nodules
3	35.3, 151.0	5560	87	0.23	uniform light brown color, manganese nodules, stiff/sticky texture of sediments below 2 cm
4	41.8, 148.2	4970	89	0.15	very light brown color, 1-3 cm fluff layer above sediment, burrows
5	49.8, 149.6	4725	80	0.57	greyish-brown color, darker between 5 and 10 cm, grittier below 5 cm, worm/tube visible

at station 4, indictive of high surface production above this station (Hou et al., 2019).

4. Material and methods

4.1. Sample collection

Sediment cores were collected using a multi-coring device (10 cm ID) and sectioned every 1 cm between 0 and 10 cm and 2 cm between 10 and 30 cm. Sectioned mud was placed in a cold van after sectioning and later

analyzed for porosity at the USC lab by weighing aliquots before and after drying at 50 °C. Samples were then dried, gently crushed, and placed in plastic bags until analysis. Weights for sediment samples were corrected for salt contribution, based on water content and salinity.

In the water column, dissolved ^{227}Ac, ^{228}Th, and the radium quartet were collected using a dual-flow path in-situ pump (McLane WRT-LV). Each pump had two filters in parallel: the higher volume flow path had a 1 μm quartz filter (Whatman QMA) and the lower volume flow path had a 0.8 μm polyethersulfone filter (Pall Supor800). This allowed sufficient flow to pass about 1.5 m^3 during a 4-h pump. Downstream of the filter heads, flow then passed through two grooved acrylic cartridges impregnated with MnO$_2$ that sat in series. After collection, cartridges were rinsed with DIW for several minutes to remove sea-salt and then dried to 50–120% moisture using compressed air. Cartridges were re-measured multiple times from a few months to 24 months later to determine ^{227}Ac and ^{228}Ra based on the release of ^{219}Rn and ^{220}Rn progeny.

4.2. Standards and tracers

A ^{229}Th/^{225}Ac tracer (USC #89B: 9.32 ± 0.12 dpm g^{-1}) was used for measurements of ^{227}Ac in sediments, calibrated against an ^{227}Ac standard from Eckert and Zeigler diluted to an activity of 5.90 dpm g^{-1} on 4/27/2017 (See Kemnitz, 2022).

Standards for gamma counting U, ^{226}Ra, and ^{228}Ra were obtained from the Environmental Protection Agency (SRM-1 diluted pitchblende and SRM-2 diluted monzonite). All Th and Ra daughter products for the ^{238}U and ^{232}Th standards are assumed to be in secular equilibrium, with the exception of ^{210}Pb. Standards were counted in 3.0 cm high geometry, and corrections were made to account for the different sample heights that were used. For low energy gamma regions (i.e., 46 keV: ^{210}Pb), a matrix correction of 10% was routinely applied to solid phase samples when liquid solutions were used as standards based on spiking solid samples with high concentrations of known ^{210}Pb.

^{210}Pb was standardized using a NIST certified solution (SRM 4337). A few ^{210}Pb check samples were also run by alpha spectrometry using its ^{210}Po daughter and a ^{209}Po standard (USC #65D), calibrated against the NIST ^{210}Pb solution. The ^{209}Po standard was corrected for decay to the time of analysis using the recently determined half-life of 125 yr (Collé et al., 2014).

4.3. Distribution coefficients for Ra and Ac

Ac and Ra distribution coefficients (k$_d$) were determined experimentally by taking Ra-free seawater, adding deep-sea sediments, and spiking it with an aged (>45 y) ^{232}Th (USC #106A: 492 dpm g^{-1}) or ^{229}Th (USC #89E: 1500 dpm g^{-1}) solution. All daughter products in both spikes are assumed to be in secular equilibrium with their parents. ^{228}Ra (t$_{1/2}$ = 5.75 y) and ^{225}Ac (t$_{1/2}$ = 10.0 d) were used to determine Ra and Ac k$_d$ values.

The procedure for determining Ra k$_d$ values was as follows: 30 mL of Ra-free seawater was weighed and placed into 50 mL centrifuge tube (some experiments required 80 mL of seawater and used 125 mL PET bottles). Then, 1500 dpm of ^{232}Th/^{228}Ra was added to the same centrifuge tube, along with enough Na$_2$CO$_3$ to neutralize acid and bring pH between 7.5 and 7.8. Next, ~ 14 g of wet deep-sea sediments were added to tubes and shaken for at least 1 h, allowing radioisotopes to equilibrate between dissolved and solid phases. After equilibration, the tubes were centrifuged for 5 min at 2500 rpm and the seawater was decanted, filtered (0.45 μm), and a weighed aliquot passed through MnO$_2$ fibers (~1 g) 3 times. Reid et al. (1979) have shown that the absorption efficiency for Ac and Ra onto MnO$_2$ fibers are 100% in a single pass at flow rates below 1 L/ min. The fibers and wet sediments were then placed in separate polypropylene tubes and measured on HPGe detectors, using gamma rays from ^{228}Ac daughters (338 and 911 keV) to determine the ^{228}Ra activity. The final solid phase mass was

determined by drying the wet sediments and weighing the final mass (corrected for salt content).

The determination of Ac k$_d$ values was similar but required additional steps: First, a pure ^{225}Ac solution was needed. A ^{229}Th spike (matrix of 3 N HNO$_3$) was weighed out and diluted with 15 mL of 3 N HNO$_3$. ^{225}Ac was separated from ^{229}Th (and ^{225}Ra) by using a 2 mL, DGA chromatography cartridge resin from Eichrom Inc. (Martin et al., 1995). This solution was neutralized, mixed with sediments, and equilibrated as described for Ra, except that Savillex beakers were used instead of a centrifuge tube. The pH was kept between 7.3 and 7.6, to minimize ^{225}Ac sorption to the walls of the Savillex beakers. However, about 20% of the ^{225}Ac did stick to walls of the beaker after one hour of rotating the sediment slurry (this was confirmed by washing Savillex beakers with acid and measuring by HPGe). This ^{225}Ac loss did not impact our calculations because both sediment and dissolved phases were measured to determine k$_d$ values.

4.4. Alpha spectroscopy procedures

The procedure developed by Dulaiova et al. (2012) for ^{227}Ac in rocks was used, with the exception of adding Fe carrier. For these sediments, sufficient Fe is present, so this addition was not needed. Excellent separation and good yields (average of 50%) were observed for Ac in deep-sea sediments, suggesting this method works well for aluminosilicate clay material. Details of this procedure are in SI S.3.

4.5. ICP-MS procedure

Uranium, thorium, and protactinium isotopes in sediments were measured by ICP-MS (Element 2, XR type) at Lamont Doherty Earth Observatory using the procedure of Fleisher and Anderson (1991) and Anderson et al. (2012). %Mn was measured at USC by following the dissolution protocol used for alpha spectroscopy described above, diluting samples in 2% HNO$_3$ containing In tracer (1 ppb) and analyzing Mn with an Element 2 ICP-MS at mass 55 amu.

4.6. Gamma spectroscopy procedures

Sediment samples (0.5–2.0 g) were dried, gently crushed, and placed in polyethylene or polypropylene tubes (tubes were 5 cm in height and 0.5 cm in diameter). Tubes were then placed in a high purity intrinsic germanium well-type detector (HPGe ORTEC, 120 cc active volume), and counted for 2–8 days to determine ^{210}Pb (46 keV) and ^{226}Ra (186 keV). ^{235}U (185.7 keV) interference at 186 keV was removed by using the ^{238}U activity determined from ^{234}Th (63 keV) and the natural ^{235}U/^{238}U ratio. For samples near the sediment-water interface, a fraction of the ^{222}Rn produced in situ should be lost by diffusion into the overlying water column. The scale length (1/e) of the Rn loss was assumed to be 3 cm and 50% of the Rn was assumed to be mobile, based on measurements of Rn profiles in equatorial sediments (Hammond et al., 1996). Excess ^{210}Pb (^{210}Pb$_{ex}$) was determined by subtracting the measured ^{226}Ra (corrected for ^{222}Rn loss in the upper 5 cm) from total ^{210}Pb activity and correcting for decay of ^{210}Pb$_{ex}$ between collection and analysis. At depths below the bioturbated layer, ^{210}Pb and ^{226}Ra were in good agreement. A more detailed explanation of this procedure is available in SI S.4.

4.7. Core incubation

Core incubations were carried out at each station using the methodology from Hammond et al. (2004). Briefly, after retrieval of replicate cores from the multi-core device, the spring-loaded arms were released, and rubber stoppers were placed on the bottom of the cores. Next, a moveable piston was inserted into each core top, which could be advanced as water was withdrawn. Overlying height was adjusted to 12 cm and decreased as samples were taken to measure nutrient fluxes. The

incubation plug had a stirring device that continuously stirred the overlying water for the entire incubation period. Results for nutrient fluxes from these cores have been published in Hou et al. (2019).

After the incubation was completed, the remaining water from each core was siphoned out, and all water from the two replicate cores at each site was combined for measurement of ^{227}Ac and ^{228}Ra (~1.0 L). This water was passed through loose MnO_2 coated fibers (20 g), at least 3 times at <1.00 L/min to insure complete absorption of radium, thorium and actinium (Reid et al., 1979). MnO_2 fibers were then stored at room temp and shipped back to the USC lab. Upon arrival at USC, fibers were washed several times with DIW to remove sea-salt and then dried to 80–120% moisture to be analyzed for its ^{223}Ra and ^{224}Ra activity on RaDeCC (Moore and Arnold, 1996; Sun and Torgersen, 1998). Measurements began 7 to 20 days after incubation ended (longer delays for earlier stations). Subsequent measurements were made up to 2 years after collection, allowing ^{223}Ra, ^{224}Ra, ^{228}Ra, and ^{227}Ac activities at the end of the incubation period to be calculated using the Bateman equation fit to the data (Bateman, 1910; See SI S.5 for details). For the long-lived isotopes ^{227}Ac and ^{228}Ra the approach of Hammond et al. (2004) was used to calculate benthic flux J:

$$J = \Delta A \times \sum \frac{h}{t} \qquad (11)$$

where ΔA is the increase in activity (dpm m^{-3}) of ^{227}Ac or ^{228}Ra during the incubation (in practice, initial concentrations were negligible), t is time of incubation period, and h is height of the overlaying water above the sediment-water-interface (SWI) in the core. Because aliquots of water were periodically removed to use for other analyses during the incubation, h/t must be summed for each incubation interval. For short-lived isotopes, the computation is more complex because these isotopes decay during the incubation period. A parameter a_i was computed (m^{-1}) to calculate flux, with a_i based on water height and time for each incubation step, including radioactive decay (see SI).

5. Results and discussion

Estimates of benthic isotope fluxes have been made based on reaction-transport modeling of profiles of solid phase measurements, integrating profiles of daughter-parent deficiencies, and directly measuring isotope fluxes from incubated cores. Applying some of these approaches required measurements of distribution coefficients and evaluation of bioturbation and sediment accumulation rates. These approaches are detailed in sections below.

5.1. Distribution coefficients (k_d)

One important parameter needed to describe the behavior of radio-isotopes in sediments is the partition coefficient (K), which is defined as the ratio of adsorbed solute to dissolved solute and is related to the distribution coefficient k_d (Eq. (4)). While some estimates have been made for radium k_d, (Cochran and Krishnaswami, 1980; Rama and Moore, 1996; Crotwell and Moore, 2003; Colbert and Hammond, 2008; Beck and Cochran, 2013), very little data is available for ^{227}Ac. The only study to provide K values for ^{227}Ac was Nozaki et al. (1990), and those values were estimated from Ra K values from an earlier study (Cochran and Krishnaswami, 1980).

Tables 2 and 3 summarize Ra and Ac k_d values determined experimentally in this study. The range of Ra k_d values for C-Disk-IV sediments are between 1000 and 4500 mL g^{-1}. These values fall within the range of previous Ra k_d estimates for deep-sea sediments (Beck and Cochran, 2013). For Ac, k_d values are much larger, but the patterns for different stations are similar. Station 1 shows constant Ra and Ac k_d values in the upper 3 cm of sediments (1500 & 15,100 mL g^{-1}), while other stations tend toward higher values at depth. Station 2 has the highest Ra and Ac k_d values (3260 & 21,600 mL g^{-1}), while results at other stations are

Table 2
^{228}Ra k_d results using ^{232}Th spike solution. ^{228}Ra was measured in the dissolved and solid phase after rotating sediment slurry for at least one hour.

CDISK	depth	pH	mass:water	^{228}Ra k_d	# measured
Station	cm		ratio	mL g^{-1}	n
1	0.5	7.6	0.003	1381 ± 88	1
1	1.5	7.7	0.165	1456 ± 77	2
1	2.5	7.9	0.004	1590 ± 79	1
1	17	7.9	0.006	2117 ± 138	1
2	0.5	7.9	0.005	2620 ± 169	2
2	1.5	7.6	0.004	3804 ± 195	2
2	2.5	7.9	0.004	3366 ± 171	1
2	17	7.7	0.006	4438 ± 216	1
3	0.5	7.8	0.005	1133 ± 48	2
3	1.5	7.7	0.100	1464 ± 180	2
3	2.5	7.7	0.120	1364 ± 133	2
3	6.5	7.7	0.006	2357 ± 121	1
4	1.5	7.8	0.004	1521 ± 53	3
4	2.5	7.7	0.004	1540 ± 63	1
5	1.5	7.6	0.006	1210 ± 68	1

Table 3
^{225}Ac k_d results using ^{229}Th spike solution. ^{225}Ac was measured in the dissolved and solid phases after rotating sediment slurry for one hour.

CDISK	depth	pH	mass:water	^{225}Ac k_d	# measured
Station	cm		ratio	mL g^{-1}	n
1	0.5	7.4	0.003	15,532 ± 1605	3
1	2.5	7.6	0.003	14,722 ± 1257	1
2	0.5	7.5	0.003	15,931 ± 1984	2
2	1.5	7.6	0.005	25,786 ± 2408	2
2	2.5	7.6	0.005	23,000 ± 2400	1
3	0.5	7.4	0.003	6846 ± 382	2
3	1.5	7.5	0.003	7433 ± 587	2
4	1.5	7.3	0.004	5354 ± 369	2
5	1.5	7.5	0.003	3453 ± 123	2

about 2× smaller. There is a trend for decreasing k_d values with larger grain sizes that are visually apparent at stations 4 and 5. Another variable that was tested for Ra k_d values was the mass-to-water ratio. Deep-sea sediments have an in-situ mass-to-water ratio of 0.28 g mL^{-1} (ρ_s = 2.50 g mL^{-1}, ϕ = 0.90, ρ = 0.25) that is much larger than experiments. However, there was no trend witnessed with changing mass-to-water ratios on Ra k_d values (Table 2). Ac k_d experiments did not vary mass to water ratios, but this variable might be checked in future endeavors.

Stations 1 and 2 are characterized by more clay-like material, and its sediment composition has higher %Mn compared to the northern stations. Ra k_d values seem to be influenced by %Mn in these sediments, but not as noticeably as Ac (Fig. 2). Previous authors have observed that Ra and other actinides are strongly influenced by adsorption onto Mn-oxides in marine sediments (Kadko, 1980; Kadko et al., 1987; Hayes et al., 2015). %Mn differed at different C-Disk-IV stations, but at each station it was nearly constant in the upper 7.5 cm, and both Ac and Ra k_d values at each station were also fairly uniform.

Fig. 3 shows Ac vs. Ra k_d values for these experiments. It indicates that Ac k_d values are 6.6 times higher than Ra k_d values. While measurements are limited, this relationship could prove helpful in future modeling of ^{227}Ac in deep-sea sediments. Previous work has assumed that the Ac k_d value is close to that of Ra (Nozaki et al., 1990). Additional experiments (data not shown) suggest that good pH control is required, as k_d for Ac increases at higher pH.

5.2. Profiles of radioisotopes in solid phases

^{231}Pa in these sediments is largely derived from the overlying water column, where it is produced by decay of ^{235}U and scavenged by sinking particulates (Bacon and Anderson, 1982; Anderson et al., 1983). Based on ^{238}U, <0.1 dpm g^{-1} of ^{231}Pa should be supported by its ^{235}U parent in
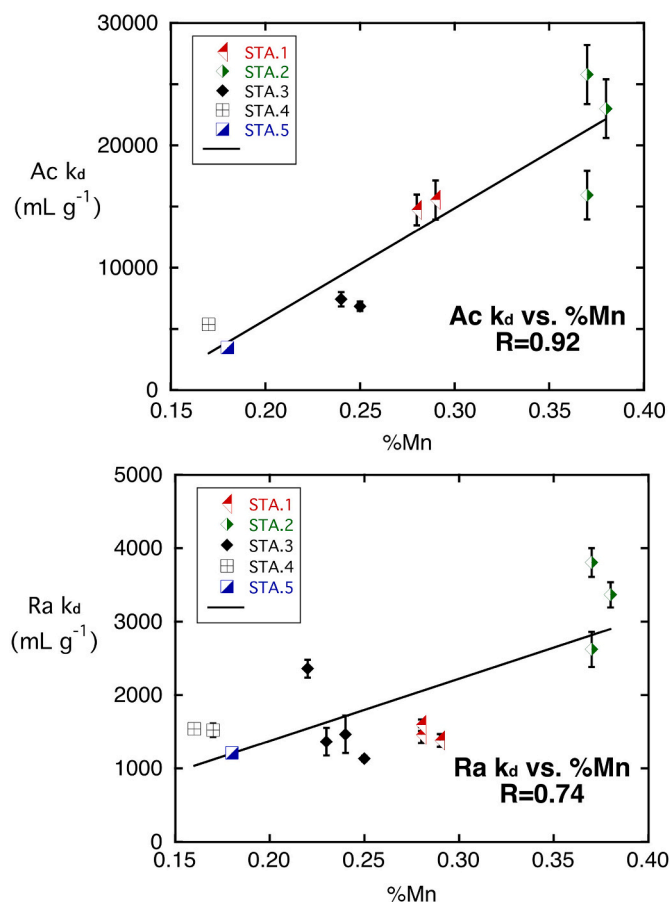
Fig. 2. Ac and Ra k_d vs. %Mn from aliquots taken from 0 to 7 cm depth for all C-Disk-IV stations. Spikes of ^{225}Ac and ^{228}Ra were added to slurries of seawater and sediments, agitated for an hour, separated, and the activities of water and solids were measured by gamma spectroscopy.
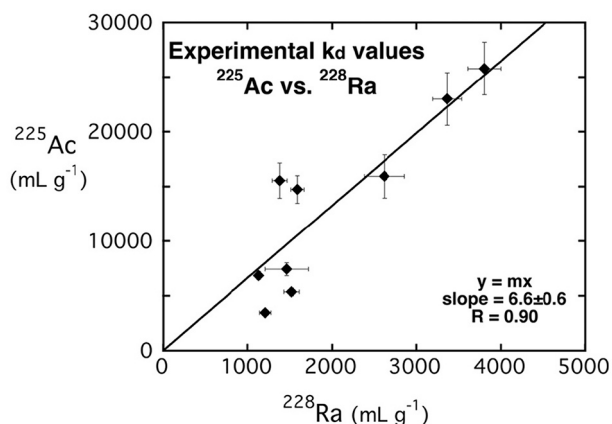

Fig. 3. ^{225}Ac vs. ^{228}Ra k_d values. The regression line is forced through zero.

sediments (See SI Table S.2 for ^{238}U activity). Fig. 4 displays ^{231}Pa concentrations in surface sediments vs. latitude in the Pacific Ocean near 150°W. Both published (Lao et al., 1992) and this study's values are shown. There is a clear trend of increasing ^{231}Pa concentrations moving south from the Aleutians, likely reflecting less dilution of ^{231}Pa raining from the overlying water column by lower fluxes of detrital sediment (note accumulation rates in Table 1). Data from two regions fall off this trend: one is located near the equatorial Pacific, where a high sedimentation rate due to preservation of CaCO$_3$ should dilute the ^{231}Pa
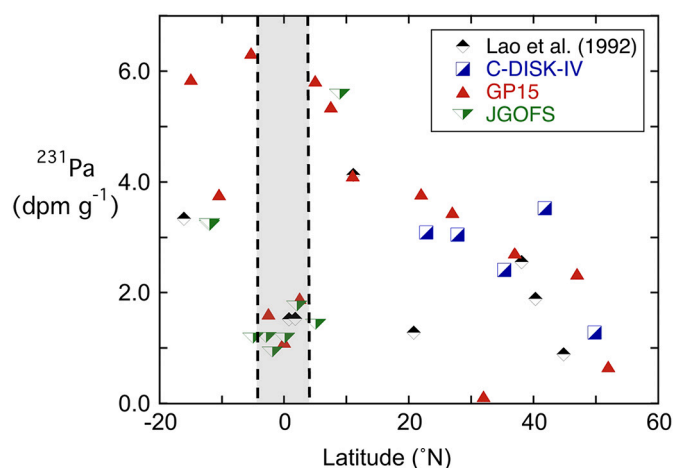

Fig. 4. ^{231}Pa activity in surface sediments vs. latitude in the Pacific Ocean (roughly along 150°W). Data taken from Lao et al. (1992), JGOFS (See SI for JGOFS data), and this study (C-Disk-IV and GP15). Equatorial stations (2.5°S - 2.5°N) have lower ^{231}Pa activities than at surrounding sites because preservation of CaCO$_3$ there dilutes the ^{231}Pa scavenged from the overlying water column. The site from the Hawaiian margin (20°N) has a lower ^{231}Pa value due to both higher sedimentation rate and shallower depth, which leads to less production of ^{231}Pa in the overlying water column. The general decrease in ^{231}Pa concentration northward of the equatorial cores reflects primarily a dilution effect from the northward increase in sediment mass accumulation rate. The low value at ~31°N (GP15 Sta 14) is believed to reflect coring of an erosional surface, and the relatively low values near 10°S may be influenced by downslope transport from adjacent topographic highs.

signal, and a second data point is near the Hawaii margin, where water depth is shallower and the ^{231}Pa rain should be smaller. The profiles of ^{231}Pa and ^{230}Th (Figs. 5, 6) suggest bioturbation mixes Pa and Th fairly well throughout the upper 5–8 cm, most likely reflecting the long half-lives of each isotope relative to the mixing time scales.

^{210}Pb$_{ex}$ profiles (Fig. 5) indicate varying bioturbation rates (D$_b$) throughout the study area. By fitting an exponential function to the ^{210}Pb$_{ex}$ profiles in the top 4 cm (8 cm at sta. 4), assuming constant biodiffusivity (D$_b$) and radioactive decay, D$_b$ can be calculated at each site (Table 4; Db = λ/μ^2, μ = attenuation factor in cm^{-1}). Stations 1, 2 and 3 show low D$_b$ rates (<0.01 cm^2 yr^{-1}) and stations 4 and 5 show high D$_b$ rates (>0.01 cm^2 yr^{-1}), likely reflecting the latitude dependence of organic matter rain to the benthic community (Tromp et al., 1995). However, most ^{210}Pb$_{ex}$ profiles have an erratic pattern: exponential decay in the upper 3 cm with a slight excess between 4 and 6 cm at some stations. The excess in the 4–6 cm horizons is evidence of non-local transport (bioturbation that is localized at certain horizons in the sediment profile), which is known to occur in deep-sea sediments (Teal et al., 2008; Smith et al., 1997; Boudreau, 1986). Station 4 has the highest ^{210}Pb$_{ex}$ values at depth (~5.5 cm). Station 2 has a relatively low inventory of ^{210}Pb in comparison to adjacent stations (Fig. 5), and its possible significance will be discussed later.

^{227}Ac is less strongly bound to solid phases than Th, Pa, and Pb, and can be transported within upper sediments by molecular diffusion and bioturbation, as it is produced by decay of its ^{231}Pa parent (Nozaki et al., 1990). Consequently, profiles are expected to increase with depth toward secular equilibrium with the parent isotope, a pattern that is generally apparent. The scale length is comparable to the scale length for ^{210}Pb$_{ex}$ at each station, which would be expected if bioturbation dominates transport, given the similar half-lives of these isotopes. There is little evidence of an ^{227}Ac deficiency at depths near 4–6 cm, in association with the non-local mixing ^{210}Pb$_{ex}$, but downward transport of a few percent of surficial material with low ^{227}Ac should have less influence on ^{227}Ac than on ^{210}Pb.

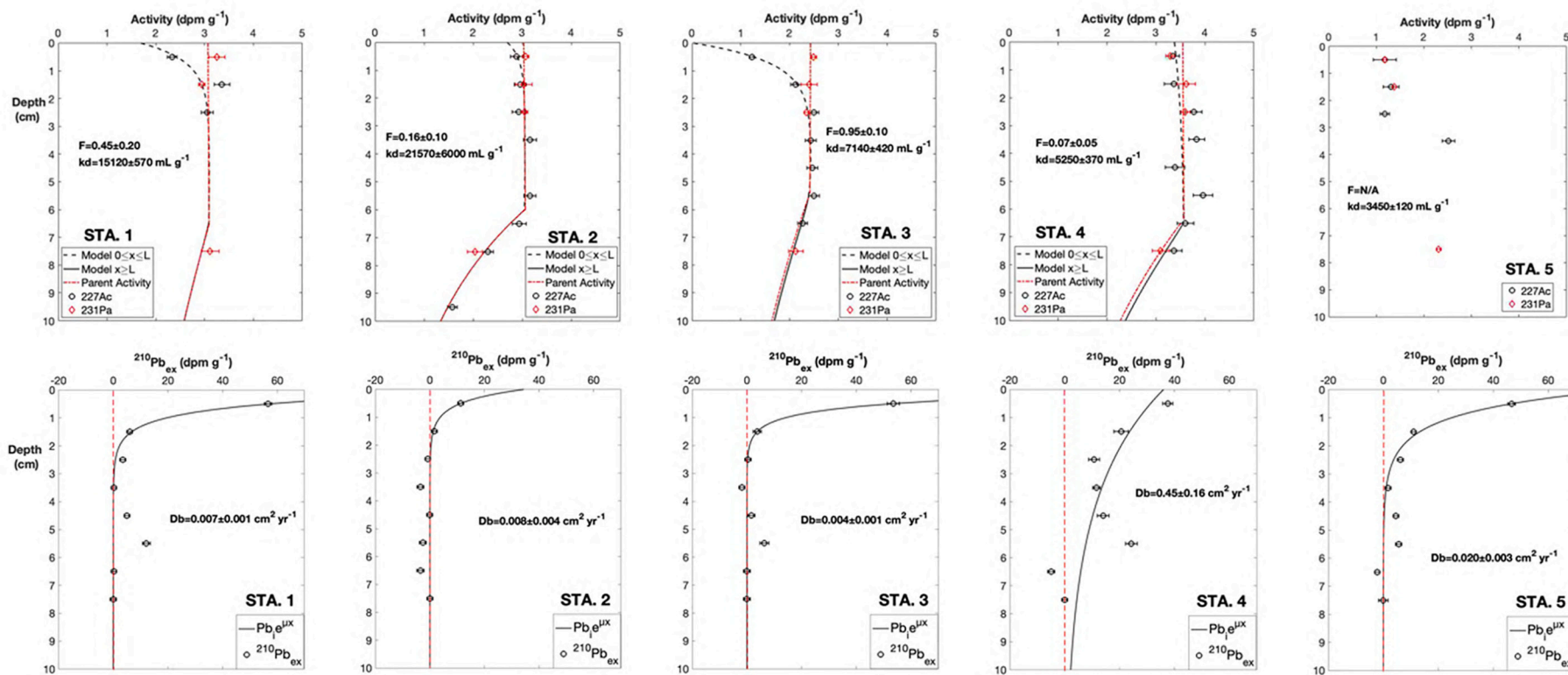While the scale lengths for ^{227}Ac do not vary enormously among the

Fig. 5. Solid phase ^{231}Pa, ^{227}Ac, and ^{210}Pb$_{ex}$ profiles for all 5C-Disk-IV stations. Eq. (6a) was fit to the solid phase ^{227}Ac profile in the upper 3 cm of sediments (Top 5 profiles). Station 5 could not be fit due to equilibrium between ^{227}Ac and ^{231}Pa in the upper 3 cm. ^{210}Pb$_{ex}$ profiles were calculated by taking the difference of total ^{210}Pb and ^{226}Ra. Measured ^{226}Ra was corrected for in situ diffusive loss of ^{222}Rn from sediments based on deep-sea profiles in the equatorial Pacific (Hammond et al., 1996). An exponential function was fit to the ^{210}Pb$_{ex}$ profiles that gave values for initial ^{210}Pb$_{ex}$ at the SWI and attenuation (μ). μ is the inverse scale length of the exponential curve and it can be used to calculate the bioturbation rate (D_b) in units of cm^2 yr^{-1}. Bioturbation is assumed constant throughout the entire ^{210}Pb$_{ex}$ profile (Bottom 5 profiles).
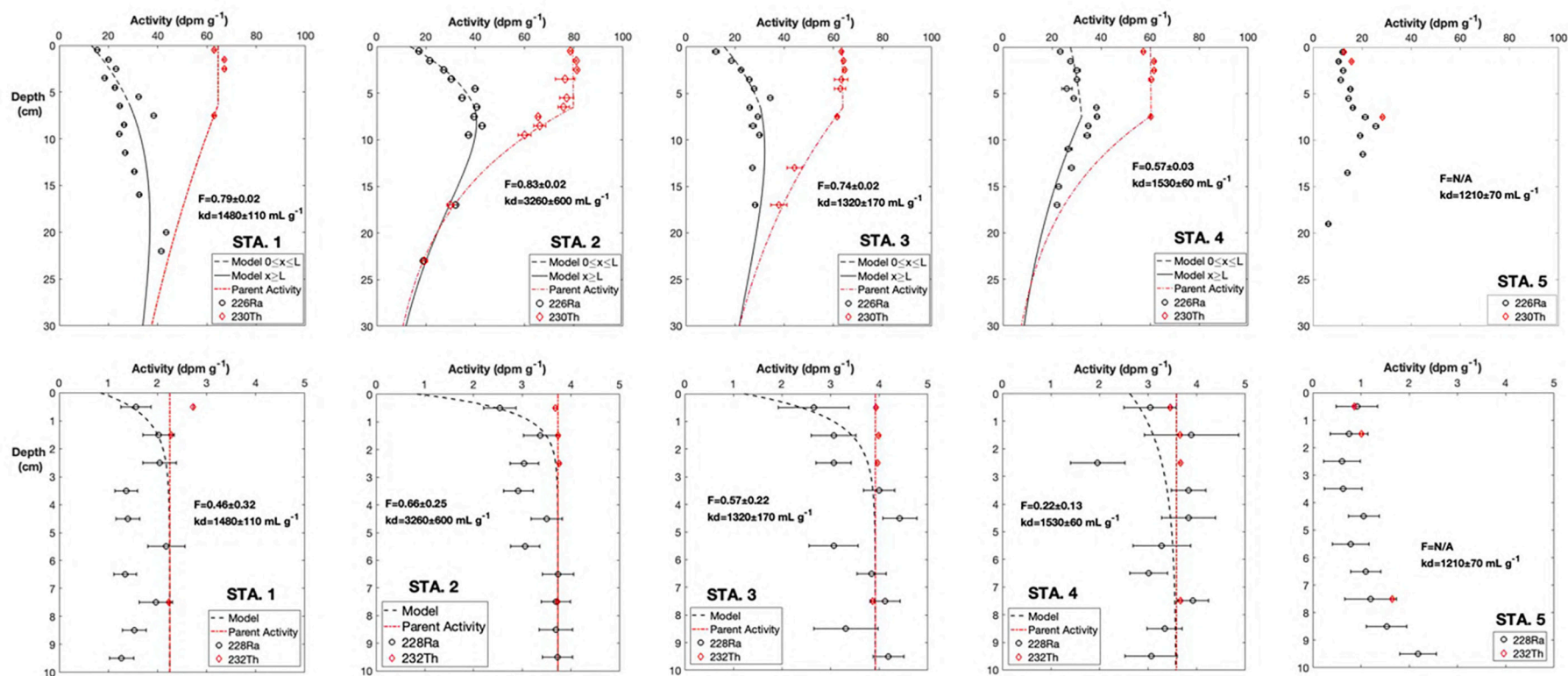
Fig. 6. Solid phase ^{230}Th, ^{226}Ra, ^{232}Th, and ^{228}Ra profiles for all 5C-Disk-IV stations. Eq. (6a) was fit to the entire solid phase ^{226}Ra profile (Top 5 profiles). Station 5 could not be fit due to equilibrium between ^{230}Th and ^{226}Ra in the upper 8 cm. The ^{228}Ra profiles were fit with Eq. (9), which is a solution to a one-layer model. All parameters such as ^{232}Th activity and D_b are assumed constant throughout the entire ^{228}Ra profile (Bottom 5 Profiles).

Table 4

Model parameters for best fit solid phase ^{227}Ac, ^{226}Ra, and ^{228}Ra profiles (Eq. (6a)). D_b, k_d, ϕ, D_m, ^{230}Th, ^{232}Th, and ^{231}Pa were all measured independently or considered known variables. S was determined from ^{226}Ra model parameters. Mixing depth (L) was determined by changes in ^{230}Th or ^{231}Pa activity at depth. Porosity (ϕ) was calculated by averaging the porosity in the upper 3 cm of sediments. Only F was allowed to vary in the model until the best fit was achieved.

Sta. #	^{231}Pa dpm g^{-1}	D_b cm^2 yr^{-1}	k_d mL g^{-1}	L cm	ϕ	D_s cm^2 yr^{-1}	S cm kyr^{-1}	F	^{227}Ac flux dpm m^{-2} yr^{-1}
1	3.09 ± 0.12	0.007 ± 0.001	15,120 ± 570	6.5	0.82	62	0.40	0.45 ± 0.20	130 ± 60
2	3.05 ± 0.10	0.008 ± 0.004	21,570 ± 6000	6.5	0.78	56	0.10	0.16 ± 0.10	40 ± 30
3	2.41 ± 0.09	0.004 ± 0.001	7140 ± 420	6.5	0.81	60	0.20	0.95 ± 0.10	290 ± 80
4	3.53 ± 0.12	0.450 ± 0.160	5250 ± 370	7.5	0.87	69	0.17	0.07 ± 0.05	90 ± 70
5	1.28 ± 0.03	0.020 ± 0.003	3450 ± 120	N/A	0.79	57	N/A	N/A	N/A

Sta. #	^{230}Th dpm g^{-1}	D_b cm^2 yr^{-1}	k_d mL g^{-1}	L cm	ϕ	D_s cm^2 yr^{-1}	S cm kyr^{-1}	F	^{226}Ra flux dpm m^{-2} yr^{-1}
1	64.9 ± 0.3	0.007 ± 0.001	1480 ± 110	6.5	0.80	85	0.40	0.79 ± 0.02	1690 ± 490
2	80.3 ± 0.4	0.008 ± 0.004	3260 ± 600	6.5	0.75	75	0.10	0.83 ± 0.02	1540 ± 780
3	64.0 ± 0.3	0.004 ± 0.001	1320 ± 170	6.5	0.78	81	0.20	0.74 ± 0.02	1580 ± 360
4	60.3 ± 0.4	0.450 ± 0.160	1530 ± 60	7.5	0.82	89	0.17	0.57 ± 0.03	720 ± 260
5	14.1 ± 0.1	0.020 ± 0.003	1210 ± 70	N/A	0.76	77	N/A	N/A	N/A

Sta. #	^{232}Th dpm g^{-1}	D_b cm^2 yr^{-1}	k_d mL g^{-1}	ϕ	D_s cm^2 yr^{-1}	S cm kyr^{-1}	F	^{228}Ra flux dpm m^{-2} yr^{-1}
1	2.25 ± 0.02	0.008 ± 0.001	1480 ± 110	0.82	89	0.40	0.46 ± 0.32	520 ± 360
2	3.73 ± 0.02	0.008 ± 0.004	3260 ± 600	0.78	81	0.10	0.66 ± 0.25	900 ± 570
3	3.92 ± 0.02	0.004 ± 0.001	1320 ± 170	0.81	87	0.20	0.57 ± 0.22	1440 ± 660
4	3.58 ± 0.02	0.450 ± 0.160	1530 ± 60	0.87	100	0.17	0.22 ± 0.13	700 ± 390
5	0.93 ± 0.02	0.020 ± 0.003	1210 ± 70	0.79	N/A	N/A	N/A	N/A

stations, there are two types of ^{227}Ac profiles found in the North Pacific: One (Sta. 1 and 3) shows a large ^{227}Ac deficiency relative to ^{231}Pa in the upper few cm of sediments, and the other (Sta. 2 and 4) shows a small deficiency in the upper few cm of sediments (Fig. 5). At all 5 stations, ^{227}Ac and ^{231}Pa activities in deeper samples show equilibrium (>5 cm), which is expected and gives confidence in the ^{227}Ac analysis procedure used here. Station 5 shows very little ^{227}Ac deficiency relative to its parent. The cause of differences among these profiles may be the result of differences in the fraction of ^{227}Ac that is mobile via molecular diffusion. However, at station 5, simple models do not account for many of the observations, and we suspect that non-steady state processes may have influenced distributions at this site. These issues are discussed further in later sections of the paper.

The ^{226}Ra profiles in the North Pacific are as expected: Most profiles of ^{226}Ra increase downcore to depths of ~8 cm (Fig. 6), reflecting transport by diffusion and bioturbation, as well as ingrowth toward equilibrium with its ^{230}Th parent. The longer scale length for ^{226}Ra reflects its longer half-life (1600 y) and lower k_d, as compared to ^{227}Ac and ^{210}Pb. Below 8 cm, ^{226}Ra shows more uniform activity until 17–20 cm, where it should approach equilibrium with its parent and decrease in activity as does its parent. Results at stations 2 and 3 establish this behavior, and it is inferred at stations 1 and 4. The ^{226}Ra profile at station 5 was somewhat erratic, with equilibrium observed between ^{226}Ra and ^{230}Th throughout the core, similar to the ^{227}Ac/^{231}Pa profile. The absence of a deficiency at this station suggests erosion of overlying sediments may have occurred in the relatively recent past (decades to centuries). This possibility is not supported by pore water profiles of silicic acid at this site (Hou et al., 2019), which do not indicate a disturbance; however, their response times to approach steady state may be only months to a few years.

Despite relatively large uncertainties, ^{228}Ra profiles show a discernible increase with depth toward equilibrium with its parent ^{232}Th (Fig. 6). Measurement of ^{228}Ra was based on its ^{224}Ra progeny detected with gamma spectrometry, which is far less precise at these low concentrations than the ICP analysis of the ^{232}Th parent. Most profiles have a small ^{228}Ra deficiency in the upper 2–3 cm of sediments. The much

smaller scale length, in comparison to ^{226}Ra, is due to its much shorter half-life ($t_{1/2}$ = 5.75 y). While the uncertainties are large, ^{228}Ra appears to be in equilibrium with its parent at depth. The activities of ^{232}Th for these profiles are constant down to 7.5 cm, except station 5, which increases in activity by 7.5 cm.

5.3. ^{230}Th and accumulation rates

S in the upper layer can also be estimated from a mass balance for ^{230}Th in the mixed layer using logic presented by Bacon (1984) and reviewed by Francois et al. (2004) and Costa et al. (2020). At steady state, the rain of ^{230}Th to sediments, divided by its production from ^{234}U in the overlying water column, can be used to define a sediment focusing factor g:

$$g = \frac{MA_r}{I} \tag{12}$$

where M = mass accumulation rate (g cm^{-2} y^{-1}). A_r = ^{230}Th in sediment raining to the sea floor and being preserved (dpm g^{-1}). I = production from ^{234}U in overlying water (dpm cm^{-2} yr^{-1}). g = (rain of ^{230}Th to sediments)/(integrated water column ^{230}Th production).

The value of g is near 1.0 in many parts of the ocean, reflecting the relatively short residence time of ^{230}Th in the water column. However, preferential boundary scavenging of ^{230}Th in high particle flux areas, sediment winnowing, or lateral inflow of water low in ^{230}Th may reduce g below 1.0. Alternatively, lateral inflow of ^{230}Th-rich water or sediment focusing at a coring site may increase g above 1.0. The rain of ^{230}Th, averaged over its lifetime, can also be estimated by integrating its downcore activity, calculated by summing its decay rate in the bioturbated mixed layer and the integration of its exponential profile based on fits below this layer in Fig. 6. Results for this approach, using cores in this study (Table 5), indicate that g is often <1. Values indicate that either notable sediment winnowing or lateral thorium transport in the water column has been occurring at stations 2, 4, and 5. However, some localized thorium removal is occurring at station 1. It is interesting to

Table 5

Mixed layer depth (L), ^{230}Th activity, inventory of ^{230}Th for upper- and lower-layer sediments and water column (Inv.), focusing factor (g), mass accumulation rates (MAR), sedimentation rate (S), and ages are shown for 5C-Disk-IV profiles. Upper and lower layers, denoted as UL and LL are referenced to layers below or above the mixing depth. Lastly, total inventory of ^{230}Th in the sediments (Tot. Inv.) and water column (WC) are shown, with g = focusing factor = (sediment inventory)/(water column production).

STA.	L	UL	UL	LL	Tot.	WC	Focusing	UL	LL	UL	LL	UL
#		^{230}Th	Inv.	Inv.	Inv.	Inv.	Factor	MAR	MAR	S	S	Age
	cm	dpm g^{-1}	dpm cm^{-2}	dpm cm^{-2}	dpm cm^{-2}	dpm cm^{-2}	g	g cm^{-2} kyr^{-1}	g cm^{-2} kyr^{-1}	cm kyr^{-1}	cm kyr^{-1}	kyr
1	6.5	65	212	1559	1771	1356	1.31	0.221	0.248	0.44	0.40	15
2	6.5	80	322	588	910	1617	0.56	0.066	0.070	0.11	0.10	61
3	6.5	64	231	905	1136	1594	0.71	0.129	0.135	0.23	0.20	28
4	7.5	60	161	496	657	1425	0.46	0.069	0.095	0.15	0.17	39
5	6.5	15	75	543	618	1355	0.46	0.345	0.204	0.57	0.25	11

note that these stations with low values of *g* are also those with much smaller values for ^{227}Ac F than expected.

An additional factor of importance for these sediments is the relatively thick bioturbated layer that exists, with ^{230}Th homogenized to depths of 6–7 cm. Rather than using ^{14}C to correct for the effective age of this layer (Francois et al., 2004), the ^{230}Th balance can be modified to include its presence and determine the residence time of ^{230}Th in this layer. The calculation assumes the excess ^{230}Th leaving the base of the mixed layer equals its input at the top (using Eq. (12)), minus decay in the mixed layer:

$$MA_m = gI - \lambda\rho L(1 - \phi_{UL})A_m \qquad (13a)$$

$$M = \frac{gI}{A_m} - \lambda\rho L(1 - \phi_{UL}) \qquad (13b)$$

where M = mass input to the upper mixed layer (g cm^{-2} yr^{-1}). A_m = activity of excess ^{230}Th in mixed layer (dpm g^{-1}). λ = decay constant of ^{230}Th (yr^{-1}). ϕ_{UL} = Upper layer average porosity.

The term on the far right of Eq. (13a) corrects for radioactive decay of ^{230}Th during passage of sediment through the bioturbated layer, and the equation can be re-arranged to find the mass accumulation rate in this layer using Eq. (13b). Below this layer, the LL (Lower Layer) MAR was derived by multiplying S determined in the LL by ρ(1-φ$_{LL}$), where φ$_{LL}$ = Lower layer porosity. Table 5 summarizes the results for mass accumulation rates (MAR) in the upper and lower layers using the above equations along with ^{230}Th inventories, sedimentation rates (S), and mixed layer age based on mixed layer mass divided by M. Most stations have similar MAR in the upper and lower layers, suggesting that the thorium dynamics have not changed significantly over the time defined by sampling (about 50 ky). The mixed layer ages here are about 10 to 60 ky.

5.4. Fitting reaction-transport models to solid phase profiles

^{227}Ac, ^{226}Ra, and ^{228}Ra profiles from C-Disk-IV stations 1–4 were fitted with the reaction-transport equations (Eqs. (6a), (9)) by using a least squares approach programmed into MATLAB. The model parameters for 'best fit' solid phase ^{227}Ac, ^{226}Ra, and ^{228}Ra profiles are summarized in Table 4. The mixing depth (L) was between 6 and 8 cm for stations 1–4 and was chosen based on profiles of the long-lived isotopes ^{230}Th and ^{226}Ra (Fig. 6). Based on averages for the mixed layer, ^{231}Pa and ^{230}Th activities were considered constant in this layer and declined exponentially thereafter, with a scale length equal to the ratio of sedimentation rate to radioactive decay as defined in Eq. (2b). A fit to the ^{226}Ra profile below the mixed layer constrained linear sedimentation rates in this zone. ^{232}Th activity was assumed constant throughout the each ^{228}Ra profile, and a one-layer model was used for these profiles as noted above (Eq. (9)).

Sedimentation rate (S) and the fraction released by parent decay (F) were allowed to be free parameters and were varied in the reaction-transport model for ^{226}Ra until the 'best fit' was achieved. The model

for ^{227}Ac and ^{228}Ra profiles used S from ^{226}Ra profiles and only varied F, the fraction of ^{227}Ac, ^{226}Ra, or ^{228}Ra that is released into pore water. Cochran and Krishnaswami (1980) predicted this value should be around 50%, since half of all alpha decays from an adsorbed parent should either release daughters into the surrounding pore waters or inject it into the solid on which it is sorbed. The fraction of Ac and Ra ejected into pore waters can either remain in solution or be reversibly adsorbed onto sediment surfaces, but it should remain mobile. The ^{226}Ra profiles had F values ranging between 50 and 80%, while ^{228}Ra had F values between 25 and 70% (Table 4). The ^{228}Ra F values are surprisingly high, assuming most of its ^{232}Th parent is probably contained in crystalline lattices. The ^{227}Ac F values had a much broader range. Stations 2 & 4 had F values below 20% while the station 3 F value was above 90%. Only station 1 had an F value around 50%. Both ^{227}Ac and ^{226}Ra should be primarily produced from their adsorbed parents, and the much lower F values for ^{227}Ac at stations 2 and 4 are unexpected.

The analytical solution for Eq. (1a) to find the isotope profiles described by Eq. (3a) and (3b) required the assumption that porosity was constant in each layer. However, changes in porosity with depth do occur; these affect the diffusivity of solutes (D$_s$) and the ratio of sorbed to dissolved solute (K). To evaluate this effect on ^{227}Ac behavior, the reaction-transport equation (Eq. (1a)) was applied numerically in a MATLAB script. The most rapid porosity change occurs in the uppermost portion of sediments (~3 cm), where the ^{227}Ac deficiency is observed (See SI S.6 for full details of model). F values and ^{227}Ac fluxes calculated for the numerical model were slightly (~20%) lower than the reaction-transport model, smaller than the uncertainties, suggesting that changes in porosity in the upper-most centimeters of sediments do not have a major effect on the reaction-transport model fits that assumed porosity is constant.

5.5. Core incubation

The ^{227}Ac and ^{228}Ra concentrations in overlying water collected during core incubations were determined by using RaDeCC to monitor the activity of ^{223}Ra and ^{224}Ra in these samples over a 3-year period. As mentioned earlier, ^{223}Ra is the granddaughter of ^{227}Ac, with a half-life of 11 days and is much more soluble than its ancestors ^{227}Th and ^{227}Ac, producing a higher flux during the incubation. Consequently, ^{223}Ra on these MnO$_2$ fibers was initially in excess over its ancestors but grew into equilibrium with its grandparent activity by 120 days. ^{224}Ra and ^{228}Ra show a similar pattern, but over a much longer time scale. Fig. 7 shows Bateman equation fits to the ^{223}Ra and ^{224}Ra activity for a typical station.

Table 6 summarizes the results for stations 1–4. Results for station 5 indicated unreasonably high fluxes (> 500 dpm m^{-2} yr^{-1}). In part, this can be attributed to a short incubation time that would result in large uncertainty, but it might reflect a problem with filtration or perhaps a non-steady state distribution of its ^{227}Ac parent profile in the sediments, as discussed earlier. If an erosional event removed surficial sediments during a time period of perhaps 1 to 20 years prior to core collection,
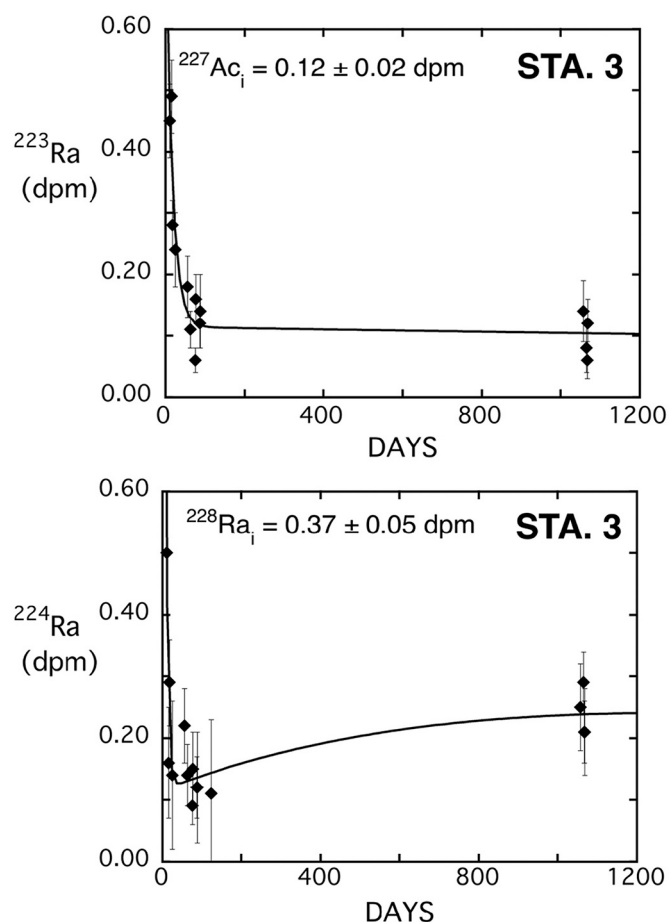
Fig. 7. Bateman equation fits to determine ^{223}Ra, ^{224}Ra, ^{228}Ra, and ^{227}Ac activities in incubation samples at the conclusion of the incubation. Samples were stored and counted for up to 3 years while ^{223}Ra and ^{224}Ra grew into equilibrium with their longer-lived ancestors. Only one station is shown for reference (STA. 3). ^{223}Ra grows into equilibrium with its grandparent activity, ^{227}Ac, by 125 days, while ingrowth of ^{224}Ra toward equilibrium with its ^{228}Ra parent is still continuing. Samples from most stations had very little excess ^{224}Ra activity due to long wait times between collection and counting (^{224}Ra: $t_{1/2} = 3.4$ days).

surficial sediments with high ^{227}Ac/^{231}Pa would be present, supplying a high, but transient, diffusive flux of ^{227}Ac.

5.6. Summary of ^{227}Ac inputs throughout the NEPB

Fig. 8 summarizes ^{227}Ac fluxes determined by all the methods discussed in this paper, including calculation of the observed ^{227}Ac deficiency (See SI S.5 for full details). Briefly, the observed deficiency was calculated by taking the difference of parent-daughter activity downcore and summing the deficiency; this method along with core incubation

approach should be the most accurate methodology for determining ^{227}Ac fluxes, since all variables are known in these two methods. Given the uncertainties, these approaches agree at most C-Disk-IV stations, as do the fluxes based on the numerical and reaction-transport (analytical) models. Although the incubation-based fluxes are often slightly less precise, they typically agree within about 35% of the mean for the first two approaches. Furthermore, the analytical model results are comparable to the numerical approach. This suggests that a simple model that accounts for major processes governing a radionuclide in marine sediments can describe solid phase ^{227}Ac profiles fairly well.

To test the accuracy of these ^{227}Ac benthic inputs, they can be compared to water column inventories of excess ^{227}Ac, computed along the GP15 transect (See SI Table S-3). The ^{227}Ac sediment fluxes are an average of the results from the core incubation and observed deficiency methods. Water column fluxes were averaged from GP15 station observations. The computation and interpretation of the water column data is the subject of a companion paper (Kemnitz et al., in prep). However, it is clear that the results are comparable within the uncertainties (~20%). Sediment fluxes for ^{227}Ac show a localized maximum at station 3 and a pronounced drop toward the north (sta. 5). Changes in the water column inventory are less apparent, but clearly are lower at the northern end of the transect. Lateral mixing in the water column is likely to mute spatially varying inputs from sediments, and these patterns will be discussed in the companion paper.

Bioturbation (D_b), Fraction released (F), and ^{231}Pa should be the major controls on ^{227}Ac fluxes in the NEPB (Nozaki et al., 1990). There is a positive correlation between ^{227}Ac fluxes and F, while there is little correlation between ^{227}Ac fluxes and k_d or ^{231}Pa (Fig. 9). The large variation in F values in the NEPB masks the correlation of ^{227}Ac fluxes with the other variables. Despite the low value for F at Station 4, its high flux reflects its large bioturbation rate, which is 50 times greater than any other station in the NEPB (Guinasso and Schink, 1975; Kadko and Ross Heath, 1984; Nozaki et al., 1990). Perhaps non-local burial of young surface material that should be deficient in ^{227}Ac has played some role in exhuming deeper material that is less deficient in ^{227}Ac. At station 2, as noted previously, the inventory of ^{210}Pb is relatively low near the surface. This might reflect a recent erosion event of the top ~1 cm at that site, perhaps a decade ago, so that pore water profiles (Hou et al., 2019) have re-adjusted, but ^{210}Pb and ^{227}Ac have not returned to steady state.

5.7. Summary of ^{226}Ra inputs throughout the NEPB

Similar to ^{227}Ac fluxes in this region, ^{226}Ra fluxes are lower north of 40°N and then increase below this latitude (Fig. 10). The fluxes for ^{226}Ra range from 200 to 1700 dpm/m^2-yr throughout 5C-Disk-IV stations. The highest ^{226}Ra fluxes were observed between 25°N-40°N (Sta.1–3). The ^{226}Ra fluxes in this region are consistent, averaging around 1350 dpm m^{-2} yr^{-1} (observed deficiency). North of 40°N, ^{226}Ra fluxes decrease toward the Alaskan margins (650–200 dpm m^{-2} yr^{-1}). Topography steps up a few hundred meters of elevation around 40°N, which is the boundary of the Mendocino Fracture Zone (MFZ) (Hautala, 2018). North
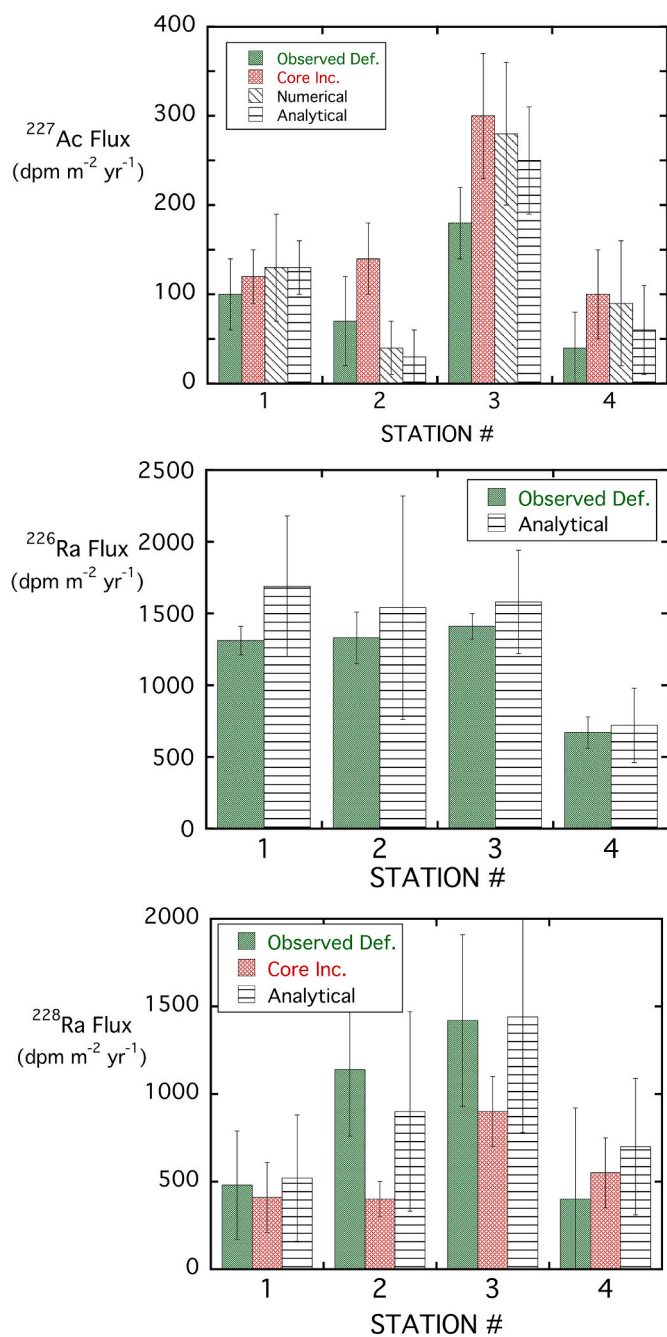
Table 6
Fluxes derived from Bateman equation fits to the core incubation samples measured over 1200 days. These fits provided the ^{227}Ac, ^{223}Ra, and ^{228}Ra activity in the core-top water at the conclusion of the incubation. Time/height is the summation of time incubated divided by height of the remaining water in the core for all segments of the incubation. Volume indicates the amount of seawater that was passed through the Mn-fibers. a_i is the effective inverse height needed to calculate flux for a short-lived radioisotope (see SI S.2). ^{227}Ac, ^{223}Ra, and ^{228}Ra fluxes were calculated by Eq. (11).

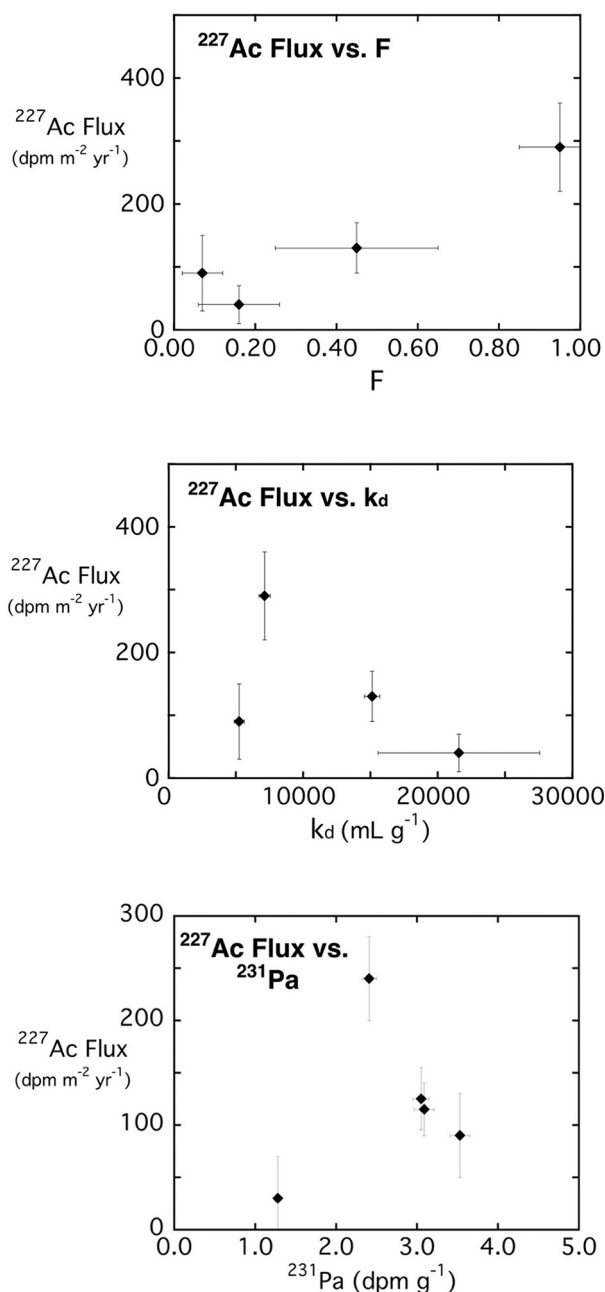| Sta.	time/height	Vol.	^{227}Ac	^{223}Ra	^{228}Ra	^{227}Ac flux	^{228}Ra flux	a_i	^{223}Ra flux
	days m^{-1}	L	dpm	dpm	dpm	dpm m^{-2} yr^{-1}	dpm m^{-2} yr^{-1}	m^{-1}	dpm m^{-2} yr^{-1}
1	142	1.35	0.07 ± 0.01	0.83 ± 0.12	0.22 ± 0.06	120 ± 30	410 ± 200	5.60	2430 ± 850
2	171	1.29	0.09 ± 0.03	0.90 ± 0.22	0.24 ± 0.07	140 ± 40	390 ± 130	6.49	2400 ± 620
3	128	1.16	0.12 ± 0.02	0.82 ± 0.17	0.37 ± 0.05	280 ± 60	880 ± 220	5.49	2870 ± 560
4	95	1.00	0.03 ± 0.01	0.41 ± 0.06	0.15 ± 0.05	100 ± 50	650 ± 220	4.35	2080 ± 920
5	51	1.00	0.12 ± 0.02	0.48 ± 0.06	0.21 ± 0.05	850 ± 110	850 ± 490	2.70	3980 ± 1200

Fig. 9. ^{227}Ac Flux vs. F, k_d, and ^{231}Pa for C-Disk-IV sediments. The results for F and k_d are taken from the reaction-transport model and ^{231}Pa is ^{231}Pa activity in the mixed layer.

Fig. 8. Top: ^{227}Ac flux was determined by all methods described in this manuscript: subtracting ^{227}Ac and ^{231}Pa from each sediment horizon in the top 3 cm of sediments (observed deficiency), curve fitting solid phase ^{227}Ac vs. depth using Eq.(6a) (reaction-transport model), creating a model that accounts for varying porosity downcore (numerical model), and direct measurements via core incubation (core incubation). Observed deficiency and core incubation should give the most accurate results. **Middle:** ^{226}Ra flux was determined by two methods: observed deficiency and curve fitting solid phase ^{226}Ra vs. depth (Eq. (6a)). **Bottom:** ^{228}Ra flux was determined by observed deficiency, core incubation, and curve fitting solid phase ^{228}Ra vs. depth (Eq. (9)). Note that core incubation results are most precise for this isotope.

of this boundary, ^{226}Ra and ^{227}Ac fluxes are much lower, likely due to the shoaling of bottom depths and increase in sedimentation, factors which should both decrease the ^{231}Pa and ^{230}Th concentrations in sediments.

These estimates are in good agreement with the ^{226}Ra sediment flux data from Cochran and Krishnaswami (1980), which reported ^{226}Ra

fluxes between 800 and 2000 dpm m^{-2} yr^{-1} for the North Equatorial Pacific. They noted that the local ^{226}Ra in the overlying water column required a benthic input of only 600 dpm m^{-2} yr^{-1}, indicating that North Equatorial Pacific was a net source of ^{226}Ra to the world's oceans. For our study area, the ^{226}Ra sediment fluxes required to explain the average standing crop of ^{226}Ra in the water column above the C-Disk-IV sites (See SI Table S-3) are a factor of ~2 lower than the measured sediment fluxes. Thus, the NEPB is comparable to the North Equatorial Pacific region in that ^{226}Ra has a large sediment flux that results in a net source of ^{226}Ra to other parts of the world's oceans.

5.8. Summary of ^{228}Ra inputs throughout the NEPB

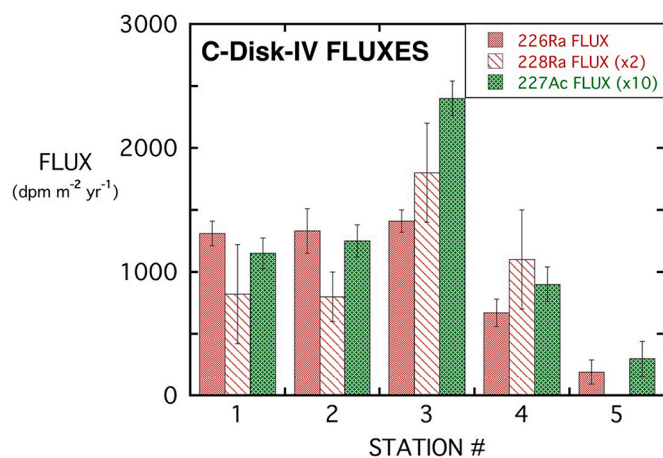Lastly, ^{228}Ra sediment fluxes were measured by core incubation and

Fig. 10. ^{226}Ra, ^{228}Ra, and ^{227}Ac Flux vs. Station # for C-Disk-IV sediments. The ^{228}Ra and ^{227}Ac fluxes were multiplied x2 and x10 in order to produce comparable scales, since ^{226}Ra flux was so much larger.

curve fitting solid phase ^{228}Ra profiles using Eq. (9). At most stations, results are comparable, although the core incubation method is more precise. At station 2, the model is twice the core incubation estimate (Fig. 8). However, the large uncertainty in the model calculation is not inconsistent with the more precise core incubation. The highest ^{228}Ra flux is located around 35°N and decreases south and north of this latitude (Fig. 10). Comparing the ^{228}Ra flux to both ^{226}Ra and ^{227}Ac in the NEPB, the highest fluxes occur south of the MFZ (~40°N) and then decrease toward the Alaskan margin. In the center of the NEPB, above oligotrophic waters, fluxes remain high and constant toward the Hawaiian margin. Comparing ^{228}Ra water column fluxes to the sediment flux, most C-Disk-IV stations agree with each other, except station 3 (35°N) (See SI). At station 3, the water column estimate is 60% higher than the sediment-based approach for the ^{228}Ra flux. This suggests that at some locations significant horizontal transport may be occurring. Water column distributions of ^{228}Ra will be discussed in a subsequent article.

6. Summary and conclusions

^{227}Ac, ^{226}Ra, and ^{228}Ra profiles in sediments were measured and modeled at 5 stations along the C-Disk-IV transect in the Northeast Pacific. The procedure of Dulaiova et al. (2012) was applied to these deep-sea sediments to measure ^{227}Ac and showed accurate and precise results.

Distribution coefficients (k_d) were measured for Ac and Ra in C-Disk-IV surface sediments. These Ra k_d values were comparable to previously published work, with values between 1000 and 3000 mL g^{-1}, which agree with Ra k_d values for similar sediments (Beck and Cochran, 2013). The Ac k_d values were between 3500 and 22,000 mL g^{-1} for the same sediments. There was a strong positive correlation between Ra and Ac k_d values, with Ac being almost 6.6 times higher than Ra k_d values, and both co-varying with the MnO_2 in solid phases. This is the first study to directly measure Ac k_d values in marine sediments.

Two independent approaches were carried out to quantify the source function of ^{227}Ac in the Northeast Pacific: Core incubation and solid phase measurements of ^{227}Ac by alpha spectroscopy. The latter approach used analytical and numerical reaction-transport models to describe the behavior of ^{227}Ac in sediments. Both models showed comparable results for ^{227}Ac fluxes when compared to core incubation results. ^{227}Ac profiles showed a large range in the fraction of mobile ^{227}Ac released from ^{231}Pa (called F) in the upper few cm of sediments, versus the expected F value of about 50%. The cause of this wide range is undetermined. At one site (station 2) a relatively low value of excess ^{210}Pb inventory suggests an erosion event could have occurred in recent

decades. At another site that underlies higher productivity waters (station 4), we speculate that non-steady state exhumation of ^{227}Ac-rich deeper sediment by bioturbation might play a role, but there is little other apparent evidence this is occurring. It is notable that about half of the expected ^{230}Th is missing from stations 2, 4 and 5, suggesting winnowing might be taking place at these sites, although it may also reflect lateral transport of ^{230}Th in the water column before it can be scavenged to sediments. Interestingly, these are also sites where the near-surface ^{227}Ac deficiency is much smaller than expected, possibly indicating exhumation of older sediments.

Most ^{226}Ra profiles for C-Disk-IV sediments have a large deficiency relative to ^{230}Th. At station 5, both ^{227}Ac/^{231}Pa and ^{226}Ra/^{230}Th profiles show near equilibrium throughout the upper sediments. This is evidence that sediments at this site have been disturbed during the past few decades, although the excess ^{210}Pb profile shows an exponential decrease through the upper 5 cm. At other C-Disk-IV sites, ^{226}Ra F values range between 57 and 83%, in agreement with previous results from deep Pacific sites. Benthic input from the NEPB is a net source of ^{226}Ra to the global ocean, averaging around 1400 dpm m^{-2}-yr^{-1} vs. the 600 dpm m^{-2}-yr^{-1} needed to supply the ^{226}Ra in the overlying water column inventory, demonstrating the importance of lateral transport of ^{226}Ra exported from this region.

^{228}Ra profiles along C-Disk-IV transect also had a modest deficiency relative to its parent, ^{232}Th. However, ^{228}Ra profiles were difficult to measure due to high counting uncertainties. F values obtained from ^{228}Ra profiles were similar to ^{226}Ra values. Core incubation results provided more precise estimates of benthic input for this isotope.

The largest ^{227}Ac fluxes observed are located near the center of the Northeast Pacific (~35°N) decreasing somewhat to the south. Smaller fluxes occur north of 40°N and decrease toward the Alaskan margins. ^{227}Ac fluxes are influenced by the ^{231}Pa concentration in sediments, sediment composition, and mass accumulation rate. The largest ^{226}Ra and ^{228}Ra fluxes are also located near the center of the Northeast Pacific, and ^{226}Ra fluxes remain high between Hawaii and 35°N. ^{228}Ra fluxes decrease south of 35°N. Both ^{226}Ra and ^{228}Ra fluxes decrease north of this latitude, approaching the Alaskan margin.

Finally, we note that a surprisingly large number of the 5 sites we have sampled do not perfectly match the idealized radioisotope distributions we anticipated. Inventories of ^{230}Th are about half the expected values at stations 2, 4 and 5. Station 5 isotope profiles appear to be non-steady state, with evidence of erosion in recent times. ^{227}Ac deficiencies in the top 1 cm are often smaller than a simple model predicts, suggesting that older material has been exhumed. This suggests that the NEPB sediments may experience far more disturbance than expected.

Declaration of Competing Interest

Authors have no competing interests at this time.

Data availability

Data will be made available on request.

Appendix A. Supplementary data

Supplementary data to this article can be found online at https://doi.org/10.1016/j.marchem.2022.104180.

References

Anderson, Robert F., Bacon, Michael P., Brewer, Peter G., 1983. Removal of [230]Th and [231]Pa at ocean margins. Earth Planet. Sci. Lett. 66, 73–90. https://doi.org/10.1016/0012-821x(83)90127-9.

Anderson, Robert F., Fleisher, Martin Q., Robinson, Laura F., Lawrence Edwards, R., Hoff, John A., Bradley Moran, S., Rutgers, Michiel, van der Loeff, Alexander L., Thomas, Matthieu Roy-Barman, Francois, Roger, 2012. GEOTRACES intercalibration of [230]Th, [232]Th, [231]Pa, and prospects for [10]Be. Limnol. Oceanogr. Methods 10 (4), 179–213. https://doi.org/10.4319/lom.2012.10.179.

Bacon, Michael P., 1984. Glacial to interglacial changes in carbonate and clay sedimentation in the Atlantic Ocean estimated from 230th measurements. Chem. Geol. 46 (2), 97–111. https://doi.org/10.1016/0009-2541(84)90183-9.

Bacon, Michael P., Anderson, Robert F., 1982. Distribution of thorium isotopes between dissolved and particulate forms in the deep sea. J. Geophys. Res. 87 (C3), 2045. https://doi.org/10.1029/jc087ic03p02045.

Bateman, H., 1910. Solution of a system of differential equations occurring in the theory of radioactive transformations. Math. Proc. Camb. Philos. Soc. 15, 423–427.

Beck, Aaron J., Cochran, Michele A., 2013. Controls on solid-solution partitioning of radium in saturated marine sands. Mar. Chem. 156, 38–48. https://doi.org/10.1016/j.marchem.2013.01.008.

Boudreau, B.P., 1986. Mathematics of tracer mixing in sediments; II, nonlocal mixing and biological conveyor-belt phenomena. Am. J. Sci. 286 (3), 199–238. https://doi.org/10.2475/ajs.286.3.199.

Charette, Matthew A., Morris, Paul J., Henderson, Paul B., Moore, Willard S., 2015. Radium isotope distributions during the US GEOTRACES North Atlantic cruises. Mar. Chem. 177, 184–195. https://doi.org/10.1016/j.marchem.2015.01.001.

Cochran, J.K., Krishnaswami, S., 1980. Radium, thorium, uranium, and ^{210}Pb in deep-sea sediments and sediment pore waters from the north equatorial Pacific. Am. J. Sci. 280 (9), 849–889. https://doi.org/10.2475/ajs.280.9.849.

Colbert, Steven L., Hammond, Douglas E., 2008. Shoreline and seafloor fluxes of water and short-lived Ra isotopes to surface water of San Pedro Bay, CA. Mar. Chem. 108 (1–2), 1–17. https://doi.org/10.1016/j.marchem.2007.09.004.

Collé, R., Fitzgerald, R.P., Laureano-Perez, L., 2014. A new determination of the [209]Po half-life. J. Phys. G Nucl. Part. Phys. 41 (10), 105103 https://doi.org/10.1088/0954-3899/41/10/105103.

Costa, Kassandra M., Hayes, Christopher T., Anderson, Robert F., Pavia, Frank J., Bausch, Alexandra, Deng, Feifei, Dutay, Jean-Claude, et al., 2020. 230Th normalization: new insights on an essential tool for quantifying sedimentary fluxes in the modern and quaternary Ocean. Paleoceanogr. Paleoclimatol. 35 (2) https://doi.org/10.1029/2019pa003820.

Crotwell, Andrew M., Moore, Willard S., 2003. Nutrient and radium fluxes from submarine groundwater discharge to port royal sound, South Carolina. Aquat. Geochem. 9 (3), 191–208. https://doi.org/10.1023/b:aqua.0000022954.89019.c9.

Dulaiova, Henrieta, Sims, Kenneth W., Charette, Matthew A., Prytulak, Julie, Blusztajn, Jerzy S., 2012. A new method for the determination of low-level Actinium-227 in geological samples. J. Radioanal. Nucl. Chem. 296 (1), 279–283. https://doi.org/10.1007/s10967-012-2140-0.

Fleisher, M.Q., Anderson, R.F., 1991. Particulate matter digestion (from mg to 10's of g) and radionuclide blanks. In: Hurd, D.C., Spencer, D.W. (Eds.), Marine Particles: Analysis and Characterization. American Geophysical Union, Washington, D.C., pp. 221–222

Francois, Roger, Frank, Martin, Michiel, M., van der Loeff, Rutgers, Bacon, Michael P., 2004. 230Th normalization: an essential tool for interpreting sedimentary fluxes during the late quaternary. Paleoceanography 19 (1). https://doi.org/10.1029/2003pa000939.

Geibert, Walter, Vöge, Ingrid, 2008. Progress in the determination of [227]Ac in sea water. Mar. Chem. 109 (3–4), 238–249. https://doi.org/10.1016/j.marchem.2007.07.012.

Geibert, W., Rutgers van der Loeff, M.M., Hanfland, C., Dauelsberg, H.-J., 2002. Actinium-227 as a deep-sea tracer: sources, distribution and applications. Earth Planet. Sci. Lett. 198 (1–2), 147–165. https://doi.org/10.1016/s0012-821x(02)00512-5.

Geibert, Walter, Charette, Matt, Kim, Guebuem, Moore, Willard S., Street, Joseph, Young, Megan, Paytan, Adina, 2008. The release of dissolved actinium to the ocean: a global comparison of different end-members. Mar. Chem. 109 (3–4), 409–420. https://doi.org/10.1016/j.marchem.2007.07.005.

GEOTRACES Planning Group, 2007. GEOTRACES – an international study of the global marine biogeochemical cycles of trace elements and their isotopes. Geochemistry 67 (2), 85–131. https://doi.org/10.1016/j.chemer.2007.02.001.

Guinasso, N.L., Schink, D.R., 1975. Quantitative estimates of biological mixing rates in abyssal sediments. J. Geophys. Res. 80 (21), 3032–3043. https://doi.org/10.1029/jc080i021p03032.

Hammond, D.E., McManus, J., Berelson, W.M., Kilgore, T.E., Pope, R.H., 1996. Early diagenesis of organic material in equatorial Pacific sediments: stoichiometry and kinetics. Deep-Sea Res. II Top. Stud. Oceanogr. 43 (4–6), 1365–1412. https://doi.org/10.1016/0967-0645(96)00027-6.

Hammond, Douglas E., Cummins, Kathleen M., McManus, James, Berelson, William M., Smith, Gerry, Spagnoli, Federico, 2004. Methods for measuring benthic nutrient flux on the California margin: comparing shipboard core incubations to in situ lander results. Limnol. Oceanogr. Methods 2 (6), 146–159. https://doi.org/10.4319/lom.2004.2.146.

Hautala, Susan L., 2018. The abyssal and deep circulation of the Northeast Pacific Basin. Prog. Oceanogr. 160, 68–82. https://doi.org/10.1016/j.pocean.2017.11.011.

Hayes, Christopher T., Anderson, Robert F., Fleisher, Martin Q., Vivancos, Sebastian M., Lam, Phoebe J., Ohnemus, Daniel C., Huang, Kuo-Fang, et al., 2015. Intensity of Th and PA scavenging partitioned by particle chemistry in the North Atlantic Ocean. Mar. Chem. 170, 49–60. https://doi.org/10.1016/j.marchem.2015.01.006.

Hou, Yi, Hammond, Douglas E., Berelson, William M., Kemnitz, Nathaniel, Adkins, Jess F., Lunstrum, Abby, 2019. Spatial patterns of benthic silica flux in the North Pacific reflect upper Ocean production. Deep-Sea Res. I Oceanogr. Res. Pap. 148, 25–33. https://doi.org/10.1016/j.dsr.2019.04.013.

Kadko, David, 1980. A detailed study of some uranium series nuclides at an Abyssal Hill area near the East Pacific rise at 8°45′N. Earth Planet. Sci. Lett. 51 (1), 115–131. https://doi.org/10.1016/0012-821x(80)90260-5.

Kadko, David, Ross Heath, G., 1984. Models of depth-dependent bioturbation at MANOP site H in the eastern equatorial Pacific. J. Geophys. Res. 89 (C4), 6567. https://doi.org/10.1029/jc089ic04p06567.

Kadko, David, Kirk Cochran, J., Lyle, Mitchell, 1987. The effect of bioturbation and adsorption gradients on solid and dissolved radium profiles in sediments from the eastern equatorial Pacific. Geochim. Cosmochim. Acta 51 (6), 1613–1623. https://doi.org/10.1016/0016-7037(87)90342-5.

Kemnitz, Nathaniel J., 2022. Modeling Deep Ocean Water and Sediments Dynamics in the Eastern Pacific Ocean Using Actinium-227 and Other Naturally Occurring Radioisotopes. PhD Diss.. University of Southern California.

Kipp, Lauren E., Charette, Matthew A., Moore, Willard S., Henderson, Paul B., Rigor, Ignatius G., 2018. Increased fluxes of shelf-derived materials to the central Arctic Ocean. Sci. Adv. 4 (1) https://doi.org/10.1126/sciadv.aao1302.

Ku, Teh-Lung, Luo, Shangde, 2008. Chapter 9 ocean circulation/mixing studies with decay-series isotopes. Radioact. Environ. 307–344. https://doi.org/10.1016/s1569-4860(07)00009-5.

Lao, Yong, Anderson, Robert F., Broecker, Wallace S., Trumbore, Susan E., Hofmann, Hansjakob J., Wolfli, Willy, 1992. Transport and burial rates of [10]Be and [231]Pa in the Pacific Ocean during the holocene period. Earth Planet. Sci. Lett. 113 (1–2), 173–189. https://doi.org/10.1016/0012-821x(92)90218-k.

Levier, M., Roy-Barman, M., Colin, C., Dapoigny, A., 2021. Determination of low level of Actinium-227 in seawater and freshwater by isotope dilution and mass spectrometry. Mar. Chem. 233, 103986 https://doi.org/10.1016/j.marchem.2021.103986.

Martin, P., Hancock, G.J., Paulka, S., Akber, R.A., 1995. Determination of [227]Ac by α-particle spectrometry. Appl. Radiat. Isot. 46 (10), 1065–1070. https://doi.org/10.1016/0969-8043(95)00222-y.

Moore, Willard S., Arnold, Ralph, 1996. Measurement of [223]Ra and [224]Ra in coastal waters using a delayed coincidence counter. J. Geophys. Res. Oceans 101 (C1), 1321–1329. https://doi.org/10.1029/95jc03139.

Moore, Willard S., DeMaster, David J., Smoak, Joseph M., McKee, Brent A., Swarzenski, Peter W., 1996. Radionuclide tracers of sediment-water interactions on the Amazon shelf. Cont. Shelf Res. 16 (5–6), 645–665. https://doi.org/10.1016/0278-4343(95)00049-6.

Nozaki, Yoshiyuki, 1984. Excess [227]Ac in deep Ocean water. Nature 310 (5977), 486–488. https://doi.org/10.1038/310486a0.

Nozaki, Yoshiyuki, Yamada, Masatoshi, Nikaido, Hirofumi, 1990. The marine geochemistry of Actinium-227: evidence for its migration through sediment pore water. Geophys. Res. Lett. 17 (11), 1933–1936. https://doi.org/10.1029/gl017i011p01933.

Rama, Moore, Willard S., 1996. Using the radium quartet for evaluating groundwater input and water exchange in salt marshes. Geochim. Cosmochim. Acta 60 (23), 4645–4652. https://doi.org/10.1016/s0016-7037(96)00289-x.

Reid, David F., Key, Robert M., Schink, David R., 1979. Radium, thorium, and actinium extraction from seawater using an improved manganese-oxide-coated fiber. Earth Planet. Sci. Lett. 43 (2), 223–226. https://doi.org/10.1016/0012-821x(79)90205-x.

Sanial, V., Kipp, L.E., Henderson, P.B., van Beek, P., Reyss, J.-L., Hammond, D.E., Hawco, N.J., et al., 2018. Radium-228 as a tracer of dissolved trace element inputs from the Peruvian continental margin. Mar. Chem. 201, 20–34. https://doi.org/10.1016/j.marchem.2017.05.008.

Shaw, Timothy J., Moore, Willard S., 2002. Analysis of [227]Ac in seawater by delayed coincidence counting. Mar. Chem. 78 (4), 197–203. https://doi.org/10.1016/s0304-4203(02)00022-1.

Smith, Craig R., Berelson, Will, Demaster, David J., Dobbs, Fred C., Hammond, Doug, Hoover, Daniel J., Pope, Robert H., Stephens, Mark, 1997. Latitudinal variations in benthic processes in the abyssal equatorial Pacific: control by biogenic particle flux. Deep-Sea Res. II Top. Stud. Oceanogr. 44 (9–10), 2295–2317. https://doi.org/10.1016/s0967-0645(97)00022-2.

Sun, Yin, Torgersen, T., 1998. The effects of water content and Mn-Fiber surface conditions on measurement by emanation. Mar. Chem. 62 (3–4), 299–306. https://doi.org/10.1016/s0304-4203(98)00019-x.

Teal, L.R., Bulling, M.T., Parker, E.R., Solan, M., 2008. Global patterns of bioturbation intensity and mixed depth of marine soft sediments. Aquat. Biol. 2 (3), 207–218. https://doi.org/10.3354/ab00052.

Tromp, T.K., Van Cappellen, P., Key, R.M., 1995. A global model for the early diagenesis of organic carbon and organic phosphorus in marine sediments. Geochim. Cosmochim. Acta 59 (7), 1259–1284. https://doi.org/10.1016/0016-7037(95)00042-x.

van der Loeff, Rutgers, Michiel, Lauren Kipp, Charette, Matthew A., Moore, Willard S., Black, Erin, Stimac, Ingrid, Charkin, Alexander, et al., 2018. Radium isotopes across the Arctic Ocean show time scales of water mass ventilation and increasing shelf inputs. J. Geophys. Res. Oceans 123 (7), 4853–4873. https://doi.org/10.1029/2018jc013888.